



Review

Modeling a 5 kW_e planar solid oxide fuel cell based system operating on JP-8 fuel and a comparison with tubular cell based system for auxiliary and mobile power applications



Tanvir Tanim^{a,*}, David J. Bayless^{b,1}, Jason P. Trembly^{c,2}

^a Department of Mechanical Engineering, Ohio University, Stocker Center 252, Athens, OH 45701, USA

^b Department of Mechanical Engineering, Ohio University, Stocker Center 265, Athens, OH 45701, USA

^c Department of Mechanical Engineering, Ohio University, Stocker Center 254, Athens, OH 45701, USA

HIGHLIGHTS

- Modeling of a 5 kW_e P-SOFC based system along with all BoP components.
- Autothermal reformer (ATR) is characterized to obtain optimum system performance.
- System efficiency of 37.1% and 29.2% are evaluated at ATR temperatures of 700 °C and 800 °C, respectively.
- Optimum operating range is suggested by conducting parametric analyses.
- A comparison study between P-SOFC and previously published T-SOFC based systems is presented.

ARTICLE INFO

Article history:

Received 7 March 2013

Received in revised form

21 June 2013

Accepted 2 July 2013

Available online 1 August 2013

Keywords:

Autothermal reformer

Solid oxide fuel cell

JP-8 fuel

Auxiliary power unit

Mobile electric power

ABSTRACT

A steady state planar solid oxide fuel cell (P-SOFC) based system operating on desulfurized JP-8 fuel was modeled using Aspen Plus simulation software for auxiliary and mobile power applications. An onboard autothermal reformer (ATR) employed to reform the desulfurized JP-8 fuel was coupled with the P-SOFC stack to provide for H₂ and CO as fuel, minimizing the cost and complexity associated with hydrogen storage. Characterization of the ATR reformer was conducted by varying the steam to carbon ratio (H₂O/C) from 0.1 to 1.0 at different ATR operating temperatures (700–800 °C) while maintaining the P-SOFC stack temperature at 850 °C. A fraction of the anode recycle was used as the steam and heat source for autothermal reforming of the JP-8 fuel, intending to make the system lighter and compact for mobile applications. System modeling revealed a maximum net AC efficiency of 37.1% at 700 °C and 29.2% at 800 °C ATR operating temperatures, respectively. Parametric analyses with respect to fuel utilization factor (*U_F*) and current density (*j*) were conducted to determine optimum operating conditions. Finally, the P-SOFC based system was compared with a previously published [1] tubular solid oxide fuel cell based (T-SOFC) system to identify the relative advantages over one another.

© 2013 Elsevier B.V. All rights reserved.

1. Introduction

The planar SOFC cell design offers several advantages over tubular cell design; especially their shorter current path, which leads to lower ohmic loss and high power density. The thin electrolyte layer in anode supported cell design allows it to operate in

the intermediate temperature region. The intermediate temperature operation is attractive as metallic interconnects can be used, which further reduce ohmic losses and increase cell longevity [2–4]. The disadvantage of intermediate temperature operation is the slower electrode kinetics causing higher activation polarization. The relatively lower exhaust temperature also makes cogeneration and hybrid systems less efficient. Furthermore, unlike seal less tubular designs, planar cells require high temperature sealants [5]. Continuous research is underway in both cell and stack level to overcome the aforementioned challenges.

While conducting system level analysis, additional complexities associated with auxiliary equipment must also be addressed. One of the major issues is associated with the system's fuel selection. The

* Corresponding author. Present address: 137 Reber Building, University Park, PA 16802, USA. Tel.: +1 740 447 3560.

E-mail addresses: tt131309@ohio.edu, trt140@psu.edu (T. Tanim), bayless@ohio.edu (D.J. Bayless), trembly@ohio.edu (J.P. Trembly).

¹ Tel.: +1 740 331 4436; fax: +1 740 593 0476.

² Tel.: +1 740 331 4921; fax: +1 740 593 0476.

Nomenclature*Roman letters*

$D_{i(\text{eff})}$	effective diffusion co-efficient of species i , $\text{m}^2 \text{s}^{-1}$
E	activation energy, J mol^{-1}
F	Faraday constant, C mol^{-1}
I	current, A
j	current density, A m^{-2}
j_0	exchange current density, A m^{-2}
K	pre-exponential factor, A m^{-2}
l	component thickness, m
LHV	lower heating value of fuel, J mol^{-1}
M_i	molecular weight of gaseous species i , kg kmol^{-1}
\dot{n}	molar flow rate, mol min^{-1}
\dot{n}_{fuel}	molar flow rate of fuel, mol min^{-1}
P	pressure, bar
P_i	partial pressure of gaseous component i , bar
P_{SOFC}	SOFC operating pressure, Pa
$P_{\text{el,DC}}$	DC power, W
$P_{\text{el,AC}}$	AC power, W
P_{comp}	compressor power, W
\bar{r}_p	mean radius of electrode pore, m
R_g	universal gas constant, $8.314 \text{ J mol}^{-1} \text{ K}^{-1}$
T_{avg}	average temperature, K
T_{op}	SOFC operating temperature, K
T_{ref}	ATR operating temperature, K
U_a	air utilization factor
U_f	fuel utilization factor
V	cell voltage, V
V_N	Nernst voltage, V

y_i molar fraction of gaseous component, i

Greek letters

$\Delta \bar{g}_f$	molar Gibbs free energy of formation, J mol^{-1}
ϵ	electrode porosity
η_{act}	activation polarization, V
η_{con}	concentration polarization, V
$\eta_{\text{el,gross}}$	gross AC efficiency, %
$\eta_{\text{el,net}}$	net AC electric efficiency, %
η_{ohm}	ohmic polarization, V
ξ	electrode tortuosity
ρ	resistivity, $\Omega \text{ m}$

Subscripts

a	anode
act	activation
c	cathode
con	concentration
e	electrolyte
eff	effective
eq	equivalent
i	gaseous component
int	Interconnect
k	second gaseous component
m	mean
ohm	ohmic

Superscripts

a	anode
c	cathode
r	reaction sites

challenge of uninterrupted H_2 supply due to expensive H_2 storage and infrastructure for SOFC operation has limited its wide spread commercial application. To overcome this challenge researchers are looking at different alternatives. One feasible alternative might be to reform an energy dense higher hydrocarbon fuel to H_2/CO rich mixture and couple it with the fuel cell stack, as SOFCs can utilize CO as a fuel. This can solve the storage issue by replacing H_2 with a high density liquid hydrocarbon fuel, which is much easier to transport and store. In such systems, apart from the SOFC stack the most important balance of plant (BoP) is the reformer which converts the hydrocarbon fuel into a H_2/CO rich mixture in a coke free operating region. In order to prevent coke production under efficient fuel reforming conditions it is absolutely necessary to properly characterize reformer operation. Several other BoP components including heaters, heat exchangers, blowers, compressors, post-combustor, etc must also be considered to evaluate the whole system's performance.

Such SOFC based systems are promising as auxiliary power units (APU) for military applications in the battle field as they meet the military's requirement of low acoustic operation [6]. These systems also have potential application in temporary and permanent military base camps for mobile electric power (MEP) [7]. SOFC based APUs which operate on JP-8 fuel would be the ideal choice for U.S. Army as JP-8 is the main logistic fuel of U.S. Army. This kinds of system can also be implemented in heavy duty trucks, refrigeration units, and recreational vehicles (RVs), with minor modifications to eliminate long and inefficient idling operation [8]. Another potential application of this system is the replacement of the existing airline APUs, thereby providing lower emissions, noise and increasing usability of exhaust heat to reduce maximum onboard electric heating load [9].

Considering the aforementioned applications, a 5 kW_e P-SOFC based system operating on desulfurized JP-8 fuel along with all the BoP components was modeled. Previously, our team published a similar 5 kW_e T-SOFC based system study [1] and the current study is a continuation of that effort. The objective of the current study is to analyze a 5 kW_e P-SOFC based system which operates on auto-thermally reformed desulfurized JP-8 fuel at steady state. The ATR was adiabatically characterized at 700 °C to 800 °C, by varying the $\text{H}_2\text{O}/\text{C}$ ratio in order to obtain optimum H_2 and CO contents in a coke free operating zone. The steam and heat supply for auto-thermal reforming was sustained by recycling a portion of the exhaust stream with fresh fuel. The P-SOFC stack temperature was maintained at 850 °C, unlike the previously published T-SOFC system, which was maintained at 910 °C. Parametric analyses were performed with respect to fuel utilization factor (U_f) and current density (j) to evaluate the system's performance at variable load conditions. Finally, the performance of the P-SOFC based system was compared with the previously published T-SOFC based system to identify their relative advantages over one another with identical total active cell surface area.

2. Model description

2.1. Model assumptions

This is a zero dimensional steady state isothermal model. All working fluids were assumed as ideal gas with no pressure drop. At this high operating temperature of SOFC, it was assumed that the lower hydrocarbons (CH_4 , C_2H_6 , C_3H_8 , etc) were internally reformed to H_2 and CO, and CO was shifted to H_2 through water gas shift (WGS) reaction due to the fact that reforming reactions are more

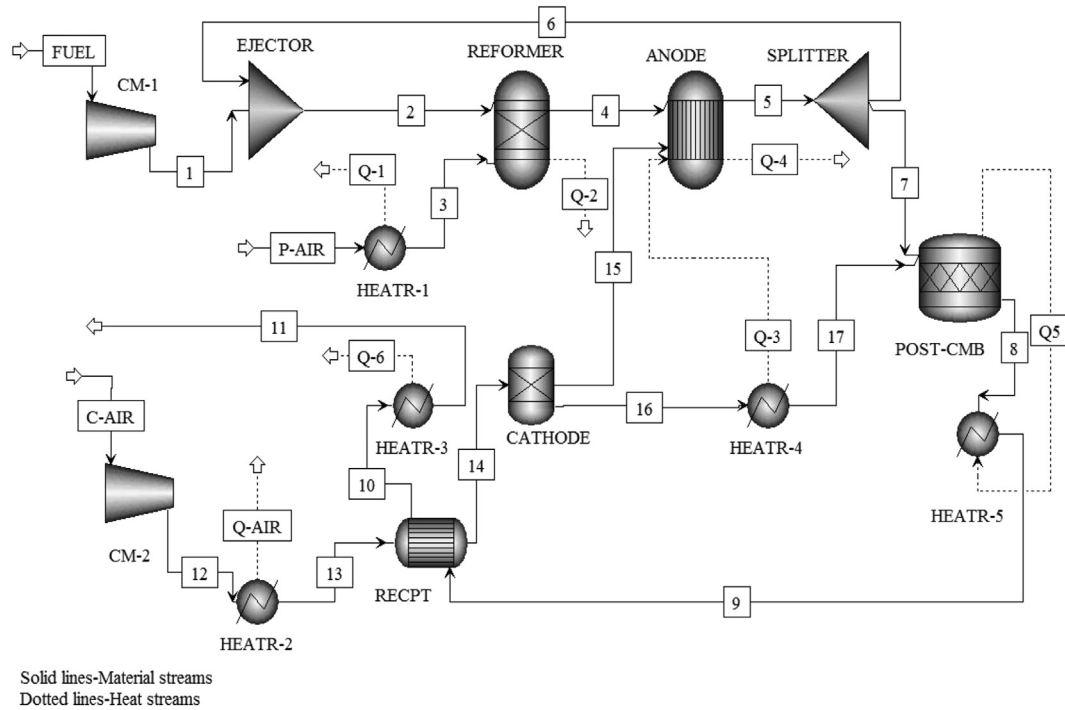
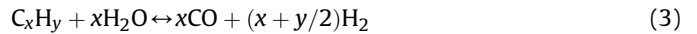
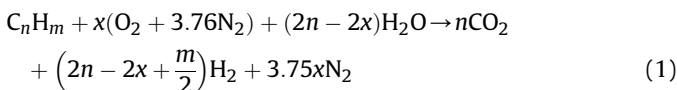


Fig. 1. 5 kW_e P-SOFC based system process flow diagram [1].

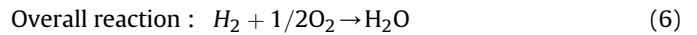
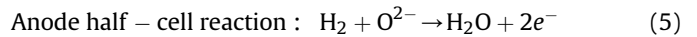
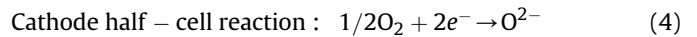
favorable than the direct oxidation of CO and CH₄. Therefore, it is common practice to assume that H₂ is the only oxidizable gas taking part in the electrochemical reaction [10,11]. It was also assumed that current flow was perpendicular to the P-SOFC plane and interconnects were metallic stainless steel (due to intermediate temperature operation) and thus ohmic voltage loss associated with the interconnects were disregarded [2,3,12].

2.2. Process flow model

The schematic view of the 5 kW_e P-SOFC based system along with all the BoP components is shown in Fig. 1. The heated fresh fuel vapor stream, 'FUEL', was compressed and mixed with the recirculated anode exhaust, splitted by a splitter module, 'SPLITTER'. A discharge pressure ratio, $P_{\text{fuel}}/P_{\text{SOFC}} = 3.0$, was maintained to allow recirculated anode exhaust flow [10,11,13]. The split fraction of the splitter module was adjusted to maintain a desired H₂O/C ratio (molar ratio of H₂O and combustible carbon entering into the 'REFORMER') at the reformer inlet. 'REFORMER', is a Gibbs reactor module which simulated the adiabatic autothermal reforming of JP-8 fuel by utilizing the incoming pre-heated air and the fuel stream mixture. The incoming air flow rate of the 'REFORMER' was controlled by using a design specification block of Aspen Plus to make the reformer adiabatic in order to achieve maximum reforming efficiency without any external heat addition [1]. At steady state, the reformer outlet stream primarily contains H₂ and CO with a small percentage of lower hydrocarbons e.g. CH₄, C₂H₆, C₃H₈, which were assumed to take part in further reforming reactions in the 'ANODE'. Eqs. (1)–(3) presented the general equations of autothermal reforming, WGS and steam reforming (SR) reactions, respectively.



The electrochemical reactions at the cell level are as follows:



As Aspen Plus was not capable of simulating the cell half reactions e.g. Eq. (4) and Eq. (5), the overall reaction (Eq. (6)) was used to simulate the electrochemical reaction using a Gibbs reactor, 'ANODE', a separator module, 'CATHODE', and a heater module, 'HEATR-4' [1,10]. The function of the 'CATHODE' block is to separate oxygen from air, based on the equivalent H₂ flow rate at the anode inlet. The equivalent H₂ flow rate was calculated assuming CO at the ATR outlet was taking part in WGS reaction (Eq. (2)) and the lower hydrocarbons were taking part in the internal reforming reactions at 'ANODE' block in the presence of steam. So, one mole of CO would produce an equivalent number of H₂ and one mole of CH₄ would produce four equivalent moles of H₂ (CH₄ + H₂O → 3H₂ + CO, CO + H₂O → H₂ + CO₂). Similarly, one mole of C₂H₆ would produce seven equivalent moles of H₂, and one mole of C₃H₈ would produce ten equivalent moles of H₂. So the total equivalent H₂ is as follows:

$$\begin{aligned} \dot{n}_{H_2,eq} &= \dot{n}_{H_2,ATR} + 1(\dot{n}_{CO,ATR}) + 4(\dot{n}_{CH_4,ATR}) + 7(\dot{n}_{C_2H_6,ATR}) \\ &+ 10(\dot{n}_{C_3H_8,ATR}) \end{aligned} \quad (7)$$

The known fuel and air utilization factors were used to calculate the amount of H₂ and O₂ consumed in 'ANODE' by using the Aspen Plus calculator block and using Eqs. (8)–(10). Note that the desired oxygen split fraction was calculated by varying the air flow rate of 'CATHODE' which consequently sets the oxygen flow rate. For more information see Ref. [1].

Table 1
Functions of Aspen Plus blocks used in this simulation.

Block Name	Block type	Block function
'CM-1', 'CM-2'	Compressor	Compress fresh fuel and air streams
'HEATR-1-4'	Heater	Heats/cool the incoming stream
'EJECTOR'	Mixer	Mixes a portion of the P-SOFC recycle stream with incoming fresh fuel
'REFORMER'	Gibbs reactor	Autothermally reform JP-8 fuel using exhaust heat, steam and incoming pre-heated oxygen
'ANODE'	Gibbs reactor	Simulates the P-SOFC stack
'SPLITTER'	Fsplitter	Maintains a desired H ₂ O/C ratio by manipulating the split fraction of P-SOFC exhaust
'POST-COMB'	Stoichiometric reactor	Simulates the post combustion stage of the unburned fuel coming out of the P-SOFC stack
'RECPT'	Heat exchanger	Preheats the incoming air stream using the high temperature exhaust stream
'CATHODE'	Separator	Separates O ₂ from air required by the reactions in the 'ANODE' block, thus simulates cathode of SOFC

$$U_f = \frac{\dot{n}H_{2,\text{consumed}}}{\dot{n}H_{2,\text{eq}}} \quad (8)$$

$$\dot{n}O_{2,\text{consumed}} = 0.5 \cdot \dot{n}H_{2,\text{consumed}} = 0.5 \cdot U_f \cdot \dot{n}H_{2,\text{eq}} \quad (9)$$

$$O_{2,\text{frac}} = \frac{\dot{n}O_{2,\text{consumed}}}{\dot{n}O_{2,\text{in}}} = U_a \quad (10)$$

The unburned fuel was combusted in the post combustion section and simulated by a stoichiometric reactor module, 'POST-COMB', and a heater module, 'HEATR-5'. The high temperature stream, '9', was used to preheat the incoming 'CATHODE' air, using a heat exchanger module, 'RECPT'. The exiting stream '10' from the 'RECPT' still contains a substantial amount of heat which can be used for cogeneration purpose. This heat was calculated employing a heater, 'HEATR-3' and setting up the exhaust stream '11' temperature to 450 °C. All the blocks and their functions are summarized briefly in Table 1.

2.3. Electrochemical modeling

Nernst equation (Eq. (11)) was used to calculate the cell voltage and the ohmic, activation and concentration losses were subtracted from the cell voltage using empirical and semi-empirical correlations obtained from literature and listed in Table 2. Ohmic loss was calculated using Eq. (12). The geometric and material properties obtained from literature are given in Table 3. Hyperbolic sine approximation of Butler–Volmer equation listed as Eqs. (13) and (14) were considered for anode and cathode activation loss calculations, respectively as considered by several other researchers [2,3,14]. Anode and cathode exchange current densities were evaluated using semi-empirical correlations, Eqs. (15) and (16). Concentration losses were calculated using Eqs. (18) and (19). The mole fractions at the reaction sites of the gaseous species were calculated by employing Eqs. (20)–(22). The anode and cathode effective diffusivities were calculated considering both binary and Knudsen diffusion co-efficients and details can be found in literature [1,15]. An Aspen Plus design specification block evaluated cell voltage using all the equations mentioned in Table 2. The input fuel flow rate was varied by using an Aspen Plus design specification

block, to obtain the desired DC power ($P_{\text{el,DC}} = VI$). Conversely, for a known current (while conducting the current density parametric analysis) an Aspen Plus calculator block determined the equivalent fuel flow rate using Eq. (25). Eqs. (26) and (27), were used to calculate the gross and net AC efficiencies compensating the compression power loss associated with air and fuel compressors. Tables 3 and 4 listed the cell parameters and the input conditions, respectively. Table 5 presents the composition of the desulfurized JP-8 fuel used in this study.

3. Model validation

A complete 3.1 kW_e cogeneration system [19] operating on biogas was selected for validation in this study which is shown in Fig. 2. This system was selected as it contains a pre-reformer and other BoP components along with the P-SOFC stack similar to the present study. The operating temperature and pressure of the anode supported planar SOFC cells were 800 °C and 1.05 bar, respectively. Biogas (60% CH₄ and 40% CO₂) was sent to the reformer, which operated at 800 °C to partially reform the fuel before being sent to the SOFC stack. Van herle et al. [19] considered the ohmic and activation loss in their study neglecting the concentration loss as considered in this study for validation purpose only. For more information about Van herle's system please refer to Ref. [19]. Table 6 shows the model input conditions of Van herle's system. Table 7 shows the comparison results between Van herle's system and the results obtained by Aspen Plus in the current study. The reformer and the anode outlet composition showed a good match. The relative error calculated in net electrical efficiency and cogeneration thermal efficiency were less than 1.14% which strongly suggested Aspen Plus's capability of modeling this type of systems. It should also be mentioned that an autothermal reformer [20] and a 100 kW ac T-SOFC based natural gas fueled cogeneration system developed by Siemens Power Generation Inc (SPGI) were validated previously and published in Ref. [1].

4. Model results

In this section the effects of ATR air inlet temperature, H₂O/C ratio and ATR operating temperature on reformer outlet composition will be analyzed. Next, the complete system performance will be evaluated along with parametric analyses. Finally, the comparison result of the P-SOFC and T-SOFC based systems will be discussed based on equal total active cell area to examine their relative performance.

4.1. Characterization of the autothermal reformer (ATR)

The ATR inlet air stream temperature was selected by running the simulations at three different temperatures e.g. 350 °C, 450 °C and 550 °C at H₂O/C = 0.1–1.0 and examining their effects on O₂/C and H₂/C ratios. Fig. 3 indicates that increasing ATR inlet air stream temperature results in a decrease of O₂/C ratio. This suggests that as the ATR receives more heat energy from the incoming air, its oxygen demand was reduced. Reduced O₂ demand by the reformer reduces N₂ fuel dilution and direct fuel oxidation and thus helped produce more H₂ and CO (CO plots are not reported here) as presented in Fig. 4. Consistent results were obtained at other ATR operating temperatures of 700 °C and 800 °C. Observing the aforementioned beneficial effects the ATR air inlet temperature was set to at 550 °C to reduce the total number of simulations associated with the system.

Coke formation is one of the major challenges of reformer operation with carbonaceous fuels. Mixing a portion of anode recycle with the incoming fresh fuel made coke formation even more probable, thus identifying a coke free operating zone was very

Table 2

Equations used to model the P-SOFC module.

$$\text{Nernst cell voltage : } V_N = -\frac{\Delta \bar{g}_f}{2F} + \frac{R_g \cdot T_{\text{avg}}}{2F} \ln \left(\frac{P_{\text{H}_2} \cdot P_{\text{O}_2}^{0.5}}{P_{\text{H}_2\text{O}}} \right) \quad (11)$$

$$\text{Ohmic loss : } \eta_{\text{ohm}} = (\rho_a l_a + \rho_e l_e + \rho_c l_c) \cdot j \quad (12)$$

Activation loss [2,3,14]:

$$\text{Anode : } \eta_{\text{act}}^a = \frac{R_g \cdot T_{\text{op}}}{F} \sinh^{-1} \left(\frac{j}{2j_{0,a}} \right) \quad (13)$$

$$\text{Cathode : } \eta_{\text{act}}^c = \frac{R_g \cdot T_{\text{op}}}{F} \sinh^{-1} \left(\frac{j}{2j_{0,c}} \right) \quad (14)$$

$$\text{Anode exchange current density [2, 3]: } j_{0,a} = K_{a-\text{H}_2} \cdot (P_{\text{H}_2}/P^0) \cdot (P_{\text{H}_2\text{O}}/P^0) \cdot \exp \left(\frac{-E_a}{R_g \cdot T_{\text{op}}} \right) \quad (15)$$

$$\text{Cathode exchange current density [3, 15]: } j_{0,c} = K_c \cdot (P_{\text{O}_2}/P^0)^m \cdot \exp \left(\frac{-E_c}{R_g \cdot T_{\text{op}}} \right) \quad (16)$$

$$\text{Total activation polarization : } \eta_{\text{act}} = \eta_{\text{act}}^a + \eta_{\text{act}}^c \quad (17)$$

Concentration loss [2,12]:

$$\text{Anode : } \eta_{\text{con}}^a = \frac{R_g \cdot T_{\text{op}}}{2 \cdot F} \ln \left(\frac{y_{\text{H}_2} \cdot y_{\text{H}_2\text{O}}^f}{y_{\text{H}_2\text{O}} \cdot y_{\text{H}_2}^f} \right) \quad (18)$$

$$\text{Cathode : } \eta_{\text{con}}^c = \frac{R_g \cdot T_{\text{op}}}{4 \cdot F} \ln \left(\frac{y_{\text{O}_2}}{y_{\text{O}_2}^f} \right) \quad (19)$$

Mole fraction of the specific gas species at the reaction sites [2,12,16]:

$$y_{\text{H}_2}^f = y_{\text{H}_2} - \frac{R_g \cdot T_{\text{op}} \cdot l_a}{2 \cdot F \cdot P_{\text{SOFC}} \cdot D_{a(\text{eff})}} j \quad (20)$$

$$y_{\text{H}_2\text{O}}^f = y_{\text{H}_2\text{O}} + \frac{R_g \cdot T_{\text{op}} \cdot l_a}{2 \cdot F \cdot P_{\text{SOFC}} \cdot D_{a(\text{eff})}} j \quad (21)$$

$$y_{\text{O}_2}^f = 1 + (y_{\text{O}_2} - 1) \exp \left(\frac{R_g \cdot T_{\text{op}} \cdot l_c}{4 \cdot F \cdot P_{\text{SOFC}} \cdot D_{c(\text{eff})} \cdot P_c} j \right) \quad (22)$$

$$\text{Total concentration voltage loss : } \eta_{\text{con}} = \eta_{\text{con}}^a + \eta_{\text{con}}^c \quad (23)$$

$$\text{Actual cell operating voltage : } V = V_N - (\eta_{\text{ohm}} + \eta_{\text{act}} + \eta_{\text{con}}) \quad (24)$$

$$\text{Equivalent hydrogen flow rate : } \dot{n}_{\text{H}_2, \text{eq}} = \frac{60 \cdot I}{2F U_f} \quad (25)$$

$$\text{Gross AC efficiency : } \eta_{\text{el, gross}} = \frac{P_{\text{el, AC}}}{\dot{n}_{\text{fuel}} \cdot \text{LHV}_{\text{fuel}}} \quad (26)$$

$$\text{Net AC efficiency : } \eta_{\text{el, net}} = \frac{P_{\text{el, AC}} - P_{\text{comp}}}{\dot{n}_{\text{fuel}} \cdot \text{LHV}_{\text{fuel}}} \quad (27)$$

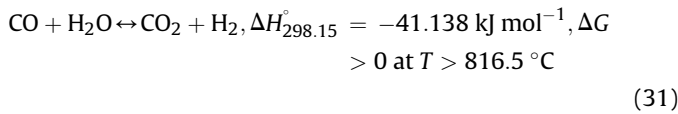
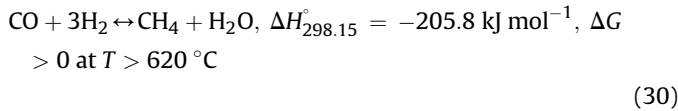
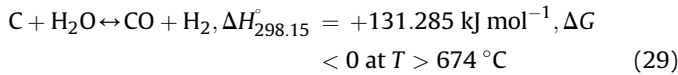
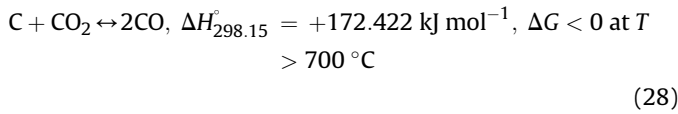
important. This was accomplished by varying H₂O/C ratio from 0.1 to 1.0 at a selected ATR operating temperature. Fig. 5 presents the effect of H₂O/C at a representative ATR operating temperature of 700 °C. The O₂/C ratio reached a maximum value at H₂O/C = 0.4 and declined marginally thereafter. At lower H₂O/C ratio in the coke

formation region, the reformer required more O₂ to provide the energy necessary for adiabatic operation. As H₂O/C ratio increased so did the recycle ratio, which provided necessary reforming heat, consequently reducing the O₂ requirement of the ATR. At lower H₂O/C ratio in the coke formation zone, the O₂ may have taken part

Table 3
Planar cell properties.

Geometry [3]:	
Anode thickness, l_a (m)	0.0005
Cathode thickness, l_c (m)	0.00005
Electrolyte thickness, l_e (m)	0.00002
Interconnect thickness, l_{int} (m)	0.0005
Cell active area, (width \times height) (m^2)	0.1×0.4
Ohmic loss [2]:	
Anode resistivity, ρ_a (Ω m)	$[95 \times 10^6 / T_{op} \exp(-1150/T_{op})]^{-1}$
Cathode resistivity, ρ_c (Ω m)	$[42 \times 10^6 / T_{op} \exp(-1200/T_{op})]^{-1}$
Electrolyte resistivity, ρ_e (Ω m)	$[3.34 \times 10^4 \exp(-10\,300/T_{op})]^{-1}$
Activation loss [2,17]:	
Pre-exponential factor, K_a/K_c ($A\,m^{-2}$)	$5.5 \times 10^8 / 7 \times 10^8$
Activation energy, E_a/E_c ($J\,mol^{-1}$)	100 000/117 000
Slope, m	0.25
Concentration loss [10,15]:	
Electrode pore radius, \bar{r}_p (m)	5×10^{-7}
Electrode porosity, ϵ /tortuosity, ξ	0.5/5.9

in the direct oxidation with solid carbon and thus produced CO. Coke formation rapidly decreased with H_2O/C due to the occurrence of the reverse Boudouard (Eq. (28)) and carbon steam reforming reactions (Eq. (29)) in the presence of H_2O and CO_2 contained in the recycle gas. This consequently produced more CO in the coke formation region. Reverse methanation reaction (Eq. (30)) also helped suppress coke formation due to its favorability at these temperatures. Higher H_2O/C also results in greater H_2 production due to more JP-8 fuel reforming and WGS reaction (Eq. (31)). H_2 production was not strong enough due to the weak thermodynamic favorability of WGS reaction in the coke free zone at these temperature ranges.

**Table 4**
Operating conditions to simulate the P-SOFC based system.

Cell operating temperature ($^\circ C$)	850
Cell pressure (bar)	1.08
Power output DC (kW)	5.5
Total active area (m^2)	3.75
Inlet fuel temperature ($^\circ C$)	265
Inlet air temperature ($^\circ C$)	25
DC to AC conversion efficiency (%)	92
Compressor efficiency (%)	80
H_2O/C	0.1–1.0
Air utilization factor U_a	0.167
Fuel utilization factor U_f	0.85
Ejector fresh fuel pressure ratio P_{fuel}/P_{SOFC}	3.0
Temperature difference between the outlet of cold and hot streams ($^\circ C$)	25
Thermal loss (%)	5

Table 5
Composition of JP-8 surrogate fuel [18].

Name	Molecular formula	Weight (%)	LHV ($kJ\,mol^{-1}$)
Iso-octane	C_8H_{18}	3.66	5064.31
<i>n</i> -Decane	$C_{10}H_{22}$	16.08	6293.01
<i>n</i> -Dodecane	$C_{12}H_{26}$	22.54	7512.24
<i>n</i> -Tetradecane	$C_{14}H_{30}$	16.87	8731.15
<i>n</i> -Hexadecane	$C_{16}H_{34}$	12.22	9949.55
Methylcyclohexane	C_7H_{14}	3.51	4256.33
Cyclooctane	C_8H_{16}	4.54	4912.24
<i>n</i> -Butylbenzene	$C_{10}H_{14}$	4.72	5563.34
1,2,3,4-Tetramethylbenzene	$C_{10}H_{14}$	4.28	5505.35
<i>m</i> -Xylene	C_8H_{10}	3.95	4330.97
Teralin	$C_{10}H_{12}$	4.14	5356.48
1-Methylnaphthalene	$C_{11}H_{10}$	3.49	5594.73

The coke free zone can be narrowed down by increasing the ATR operating temperature as presented in Fig. 6 due to high thermal decomposition of JP-8 fuel, high favorability of reverse Boudouard (Eq. (28)) and carbon steam reforming reactions (Eq. (29)) at elevated temperatures. Thermodynamic favorability of the reverse methanation reaction with temperature in the presence of steam also suppressed direct thermal cracking, thus further reduced solid coke formation as presented in Fig. 7. The minimum H_2O/C ratio required to maintain coke free ATR operation were 0.4, 0.25 and 0.15 at the respective reformer operating temperatures of 700 $^\circ C$, 750 $^\circ C$ and 800 $^\circ C$. Figs. 8 and 9 show that formation of H_2 decreased and CO increased with ATR operating temperature. This is due to the fact that at higher temperatures WGS reaction became thermodynamically unfavorable thus produced less H_2 . On the other hand the recycle stream contained more CO_2 which helped promote the reverse WGS reaction at elevated temperatures and consequently increase CO production. The rapid increase of CO in the coking region was due to the presence of coke and its conversion into CO via the reverse Boudouard, carbon steam reforming and direct oxidation reactions.

4.2. P-SOFC system performance

After characterizing the ATR, P-SOFC based system performance was investigated. The operating temperature of the P-SOFC was maintained at 850 $^\circ C$ with $U_a = 0.167$ and $U_f = 0.85$. As presented in Fig. 10, the cell voltage decreased with increasing H_2O/C ratio. This additional H_2O/C ratio increased the production of H_2 through more WGS reaction, but the average concentration of H_2 and CO at the SOFC decreased due to greater fuel dilution and caused Nernst cell voltage reduction. Lower voltage with higher H_2O/C ratio increased the current density proportionately to maintain the base DC power load. The net AC efficiency was reduced due to increased compressor power required by the increased cathode air flow rate to sustain the electrochemical reaction associated with higher H_2O/C ratio.

As discussed earlier, H_2 and CO concentrations at higher ATR operating temperatures decreased gradually due to higher fuel dilution and weak WGS reaction. The effect of this on the cell voltage and net AC efficiency can be seen in Figs. 11 and 12. In addition, higher ATR operating temperature also increased the average SOFC stream temperature, consequently reducing Gibbs' energy leading to lower cell voltage. Net AC efficiency decreased with higher ATR operating temperature at higher H_2O/C ratio due to parasitic loss attributed by the compression of higher fuel and air flow rates. Nevertheless, the system showed a maximum cell voltage of 640 mV at $T_{ref} = 700\,^\circ C$ with net AC efficiency of 37.1% at $H_2O/C = 0.4$ and a minimum cell voltage of 510 mV at $T_{ref} = 800\,^\circ C$

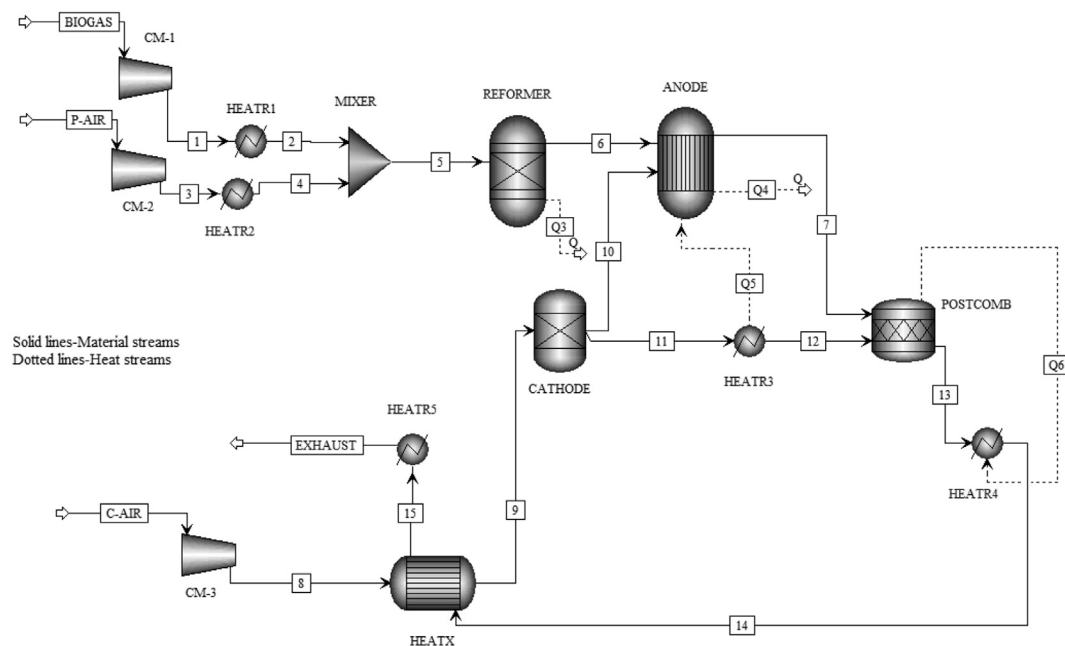


Fig. 2. Process flow diagram of Van herle et al. [19] biogas system simulated in Aspen Plus.

with net AC efficiency of 29.2% at $H_2O/C = 1.0$. Total efficiency (net AC efficiency + thermal efficiency) of the system at different ATR operating temperatures is presented in Fig. 13. Thermal efficiency of the system was calculated by keeping the exhaust stream (stream-11) temperature at 450 °C. The total efficiency of the system is dominated by the thermal efficiency at lower H_2O/C ratios as more unburned gases were able to pass through the P-SOFC to the post-combustor and combusted to release more heat. Conversely, reduction of total efficiency of the system at higher ATR operating temperatures was attributed by reduced net AC efficiency as shown in Fig. 12.

4.3. Parametric analysis

Parametric analyses were performed with respect to fuel utilization factor, U_f and current density, j , to examine the performance and robustness of the 5 kW_e P-SOFC based system at different load conditions. The lowest and highest ATR operating temperatures were maintained at 700 °C and 800 °C, at H_2O/C ratios of 0.5 and 0.3, respectively to perform the parametric analyses in the coke free region. The air utilization factor, U_a was kept constant at 0.167 for parametric analyses by varying the air flow rate.

Table 6

Input conditions of the Van herle et al. [19] system.

Fuel flow rate (Nm ³ h ⁻¹)	1.5
CH ₄ :CO ₂ in biogas	0.6:0.4
H ₂ O/C ratio (POX)	0
Inlet fuel temperature (°C)	15
Inlet air temperature (°C)	15
Reformer temperature (°C)	800
Cell operating temperature (°C)	800
Air excess ratio λ	3
Fuel utilization factor U_f	0.8
No. of cells	100
Active area (cm ²)	100
Stack operating current (A)	57
Exhaust reject state (°C)	90, vapor
Cell pressure (bar)	1.05

Fig. 14 shows that current density increased with U_f due to more H_2 consumption by the cell ($I = 2F \times nH_{2,consumed}$). Ohmic, activation and concentration losses are proportional to current density which attributed to voltage decrease with U_f . Higher fuel utilization requires more H_2 consumption at the cell level requiring less fresh JP-8 fuel to attain the required power output shown in Fig. 15. This lower fuel requirement attributed to greater net AC efficiency as shown in Fig. 14. Thermal energy increased at lower U_f as more unburned H_2 and CO were able to pass through the anode and combusted, consequently increased post-combustor outlet temperature as presented in Fig. 15.

Fig. 16 presents the effect of current density on different performance parameters of the system. Cell voltage decreased with current density due to higher polarization losses as these are directly proportional to current density shown in Fig. 17. It is also evident that activation polarization is the dominating loss in planar cell geometry due to the relatively low temperature operation (850 °C). Unlike, tubular cell design, ohmic loss is not the dominating loss for planar geometry due to smaller electron flow path. Fig. 18 shows that at higher current density operating points the required fuel flow rate, cathode air flow rate, and ATR air flow rate

Table 7

P-SOFC model simulation result comparison.

Parameters	Van herle et al. [19]	Present model
Voltage (V)	0.548	0.540
Current density, j (mA cm ⁻²)	568.2	568.5
Reformer outlet composition (mole %)	H ₂ 35.77, CO 29.62, H ₂ O 4.30, CO ₂ 3.63, CH ₄ 0.225, N ₂ 26.45	H ₂ 35.86, CO 29.75, H ₂ O 4.0, CO ₂ 3.61, CH ₄ 0.224, N ₂ 26.54
Anode outlet composition (mole %)	H ₂ 7.28, CO 5.92, H ₂ O 33.06, CO ₂ 27.41, N ₂ 26.33	H ₂ 7.44, CO 5.79, H ₂ O 32.68, CO ₂ 27.64, N ₂ 26.42
Post combustion temperature (°C)	960	962
Net electrical efficiency (%)	33.79	33.82
Cogeneration thermal efficiency (%)	57.66	58.32

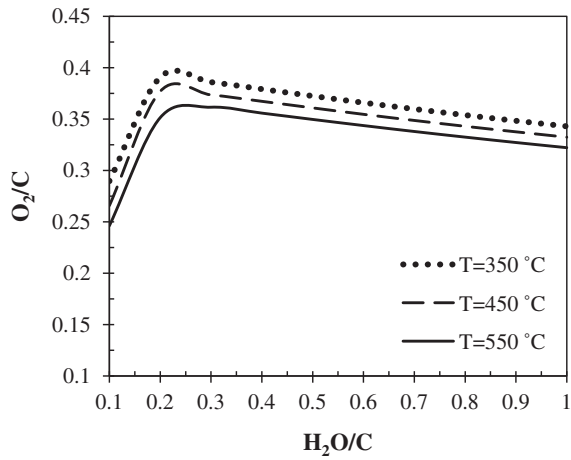


Fig. 3. Effect of ATR air inlet temperature on O₂/C ratio at $T_{ref} = 750$ °C.

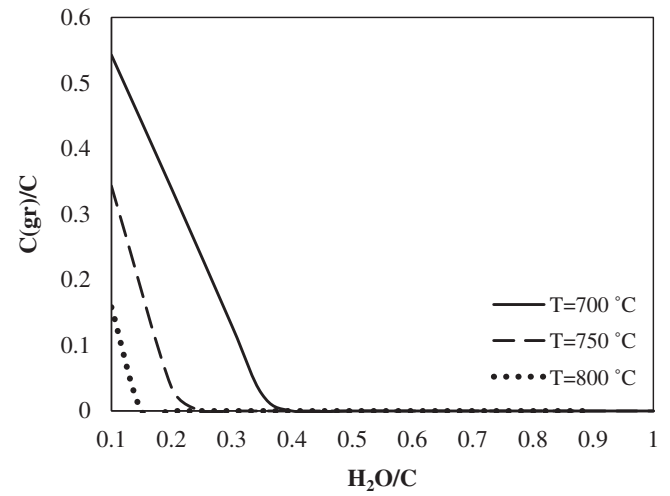


Fig. 6. C(gr)/C at different reformer temperatures.

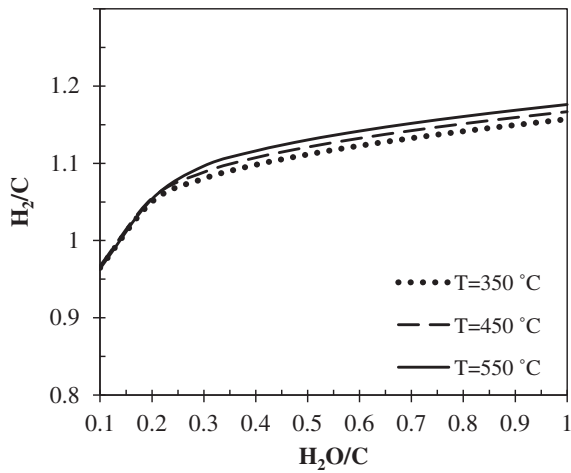


Fig. 4. Effect of ATR air inlet temperature on H₂/C ratio at $T_{ref} = 750$ °C.

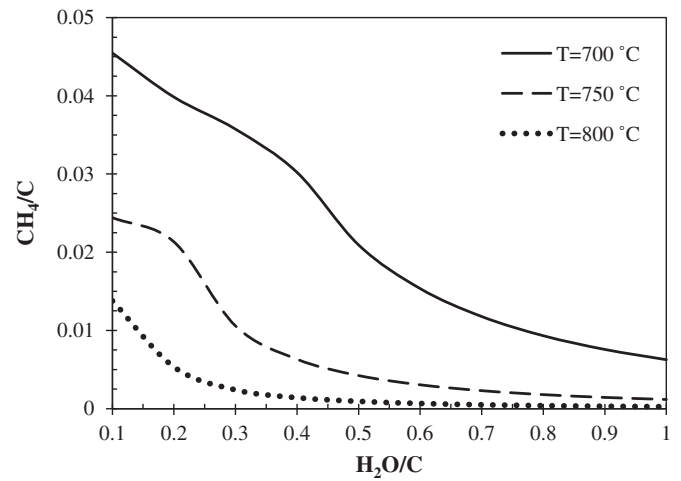


Fig. 7. CH₄/C at different ATR operating temperatures.

increased proportionately thus increasing the parasitic loss associated with the compression of those streams which consequently decreased system efficiency as presented in Fig. 16. The P-SOFC based system obtained a peak power density of 188.5 mW cm^{-2} at a

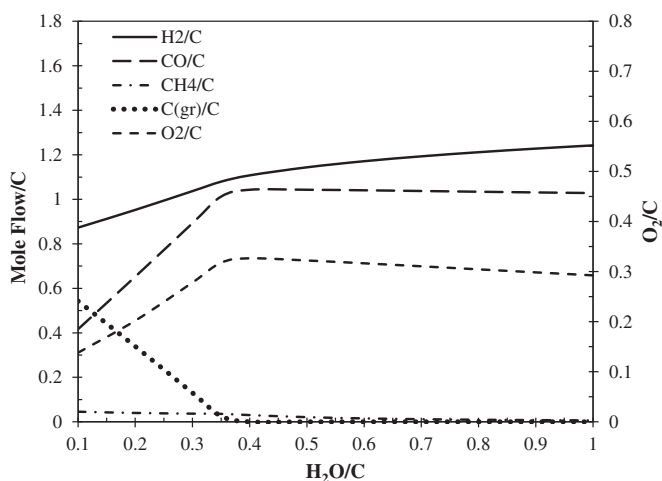


Fig. 5. ATR outlet mole flow/C for P-SOFC system at $T_{ref} = 700$ °C.

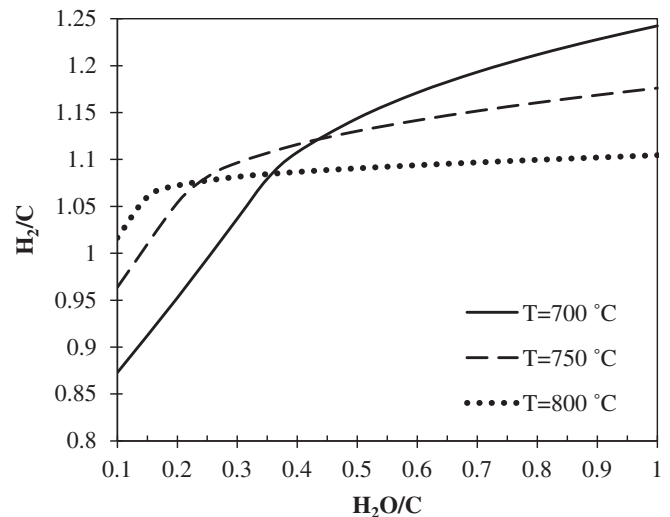


Fig. 8. H₂/C at different ATR operating temperatures.

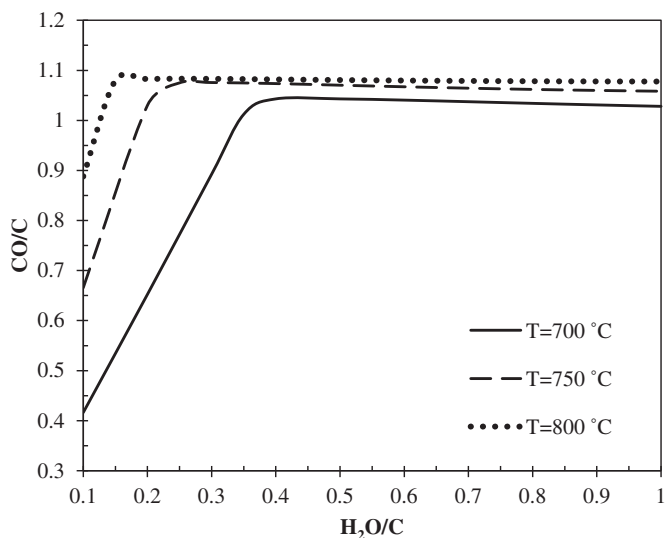


Fig. 9. CO/C at different ATR operating temperatures.

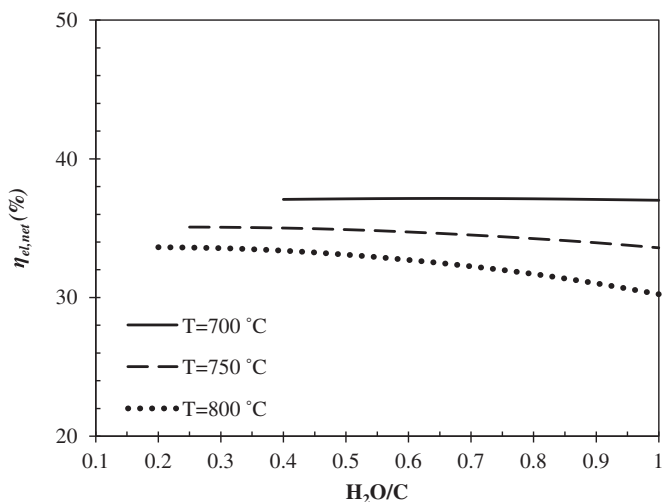


Fig. 12. Variation of net AC efficiency at different ATR operating temperatures.

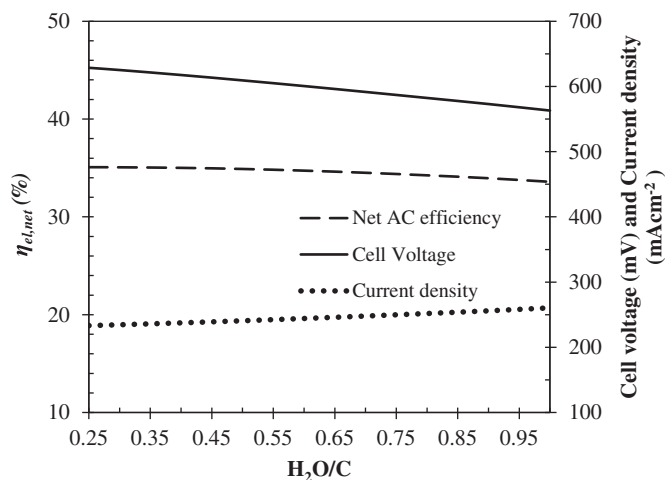


Fig. 10. Effect of H_2O/C on the cell voltage, current density and net AC efficiency at $T_{ref} = 750\text{ }^{\circ}\text{C}$.

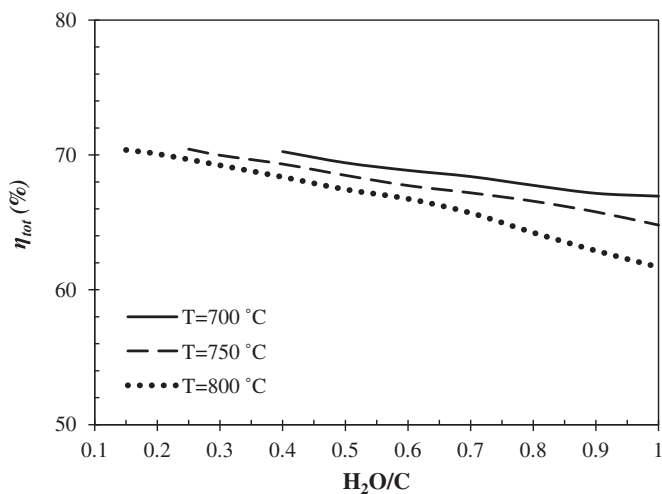


Fig. 13. Total efficiency at different ATR operating temperatures.

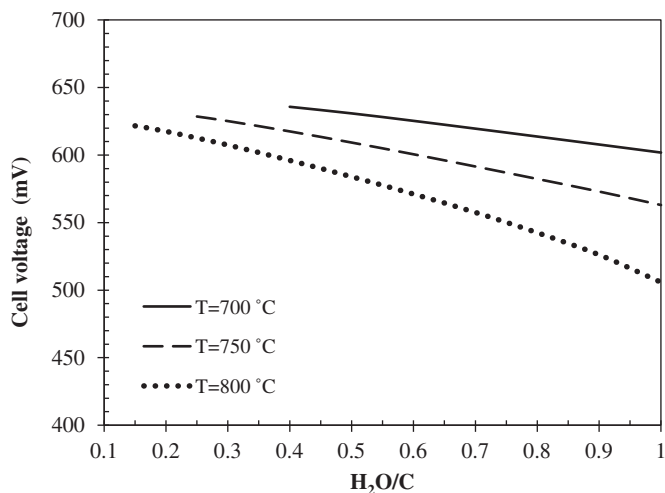


Fig. 11. Cell voltage at different ATR operating temperatures.

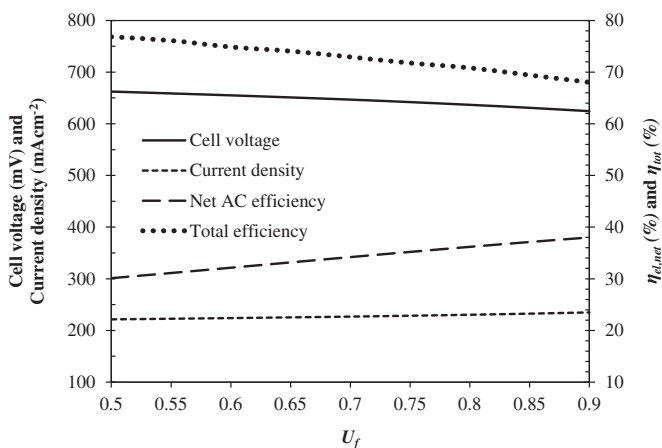


Fig. 14. Effect of U_f on voltage, efficiency and current density at $T_{ref} = 700\text{ }^{\circ}\text{C}$ and $H_2O/C = 0.5$.

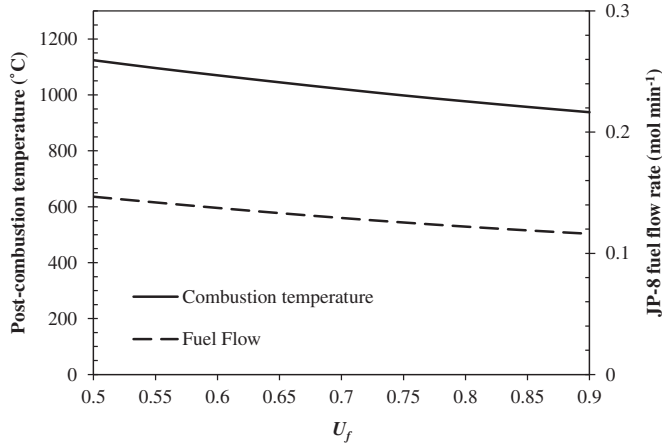


Fig. 15. Effect of U_f on post combustion temperature and anode split fraction at $T_{ref} = 700\text{ °C}$ and $H_2O/C = 0.5$.

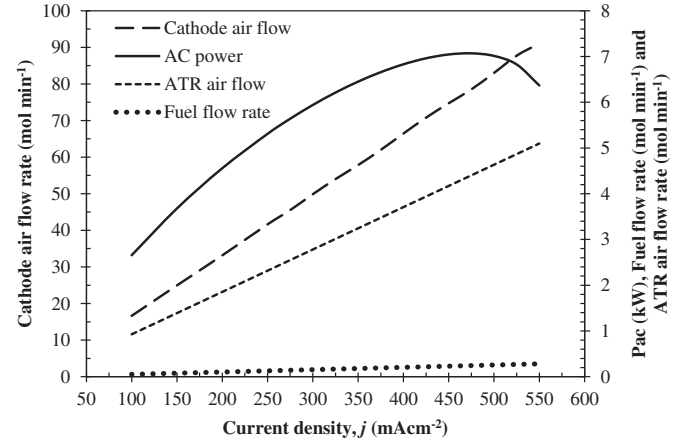


Fig. 18. Effect of current density on stack AC power, air flow rate and fuel flow rate of the system at $T_{ref} = 700\text{ °C}$ and $H_2O/C = 0.5$.

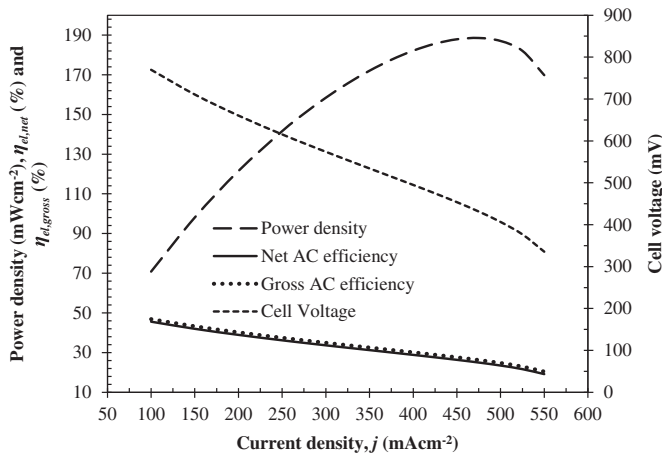


Fig. 16. Effect of current density on power density, efficiency and voltage at $T_{ref} = 700\text{ °C}$ and $H_2O/C = 0.5$.

current density of 475 mA cm^{-2} at $T_{ref} = 700\text{ °C}$ and 180.5 mW cm^{-2} at a current density of 450 mA cm^{-2} at $T_{ref} = 800\text{ °C}$. A decision considering a trade-off between operating cost and capital cost can be taken from Fig. 16 whether to operate

Table 8

Recommended current density for the P-SOFC based system.

T_{ref} (°C)	H_2O/C	j (mA cm ⁻²)	Cell voltage (V)	$\eta_{el,net}$ (%)	P_{ac} (kW)	Power density (mW cm ⁻²)
700	0.5	250–325	0.61–0.55	36.2–32.4	5.3–6.21	141.6–165.6
800	0.3		0.61–0.54	33.35–29.7	5.23–6.1	139.6–162.5

Table 9

Input conditions of the T-SOFC and P-SOFC based systems for comparison.

Active area (both tubular and planar) (m ²)	4.42
T-SOFC operating temperature, T_{op} (°C)	910
P-SOFC operating temperature, T_{op} (°C)	850
ATR operating temperature, T_{ref} (°C)	700/800
Inlet fuel temperature (°C)	265
Inlet air temperature (°C)	25
H_2O/C at 700/800 (°C)	0.5/0.3
Air utilization factor, U_a	0.167
Fuel utilization factor, U_f	0.85
Ejector fresh fuel pressure ratio	3.0
Compressor efficiency (%)	80
Temperature difference between the outlet of cold and hot stream of 'HEATX' (°C)	10
DC to AC inverter efficiency (%)	92
SOFC stack thermal loss (%)	3
Pressure drops inside the SOFC (bar)	0

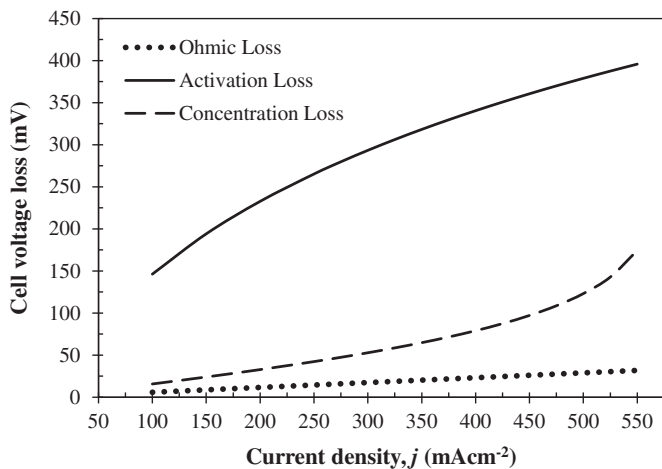


Fig. 17. Effect of current density on cell voltage loss at $T_{ref} = 700\text{ °C}$ and $H_2O/C = 0.5$.

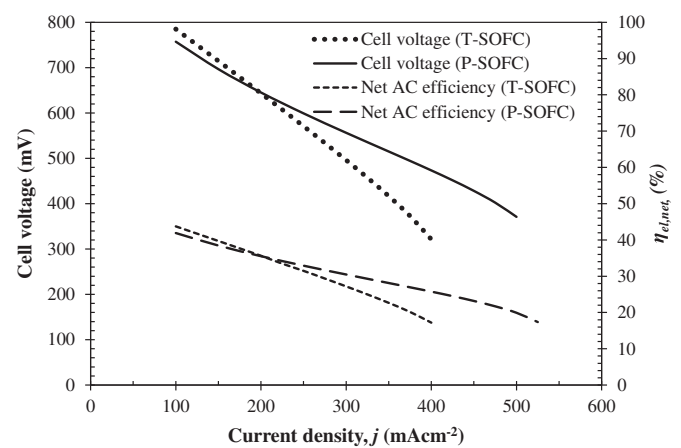


Fig. 19. Cell voltage and net AC efficiency of the two systems at different current densities at $T_{ref} = 800\text{ °C}$ and $H_2O/C = 0.3$.

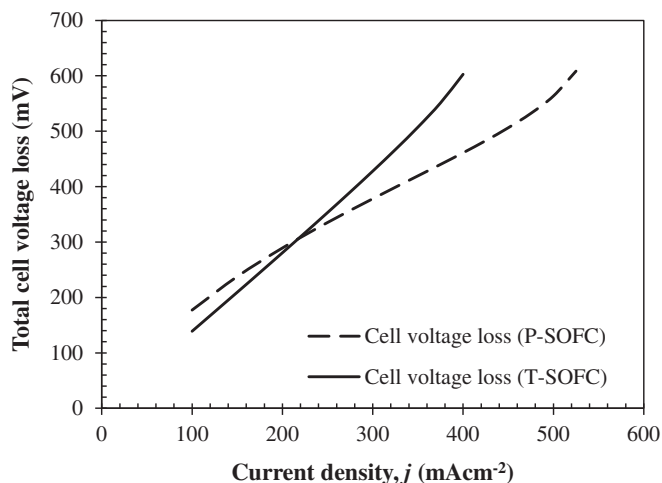


Fig. 20. Total cell voltage loss of the two systems at different current densities at $T_{ref} = 800\text{ }^{\circ}\text{C}$ and $\text{H}_2\text{O}/\text{C} = 0.3$.

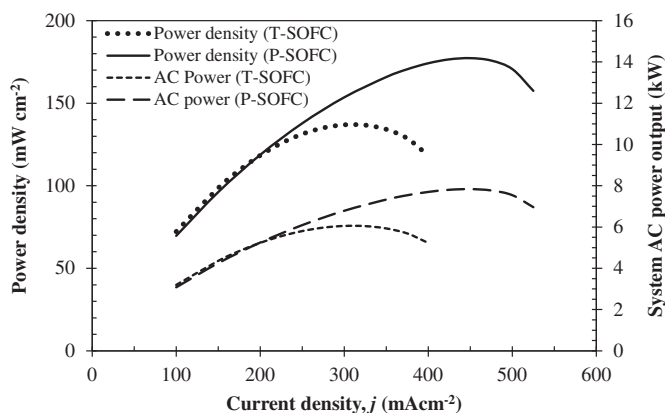


Fig. 21. Net AC power density and net AC power of the two systems at different current densities at $T_{ref} = 800\text{ }^{\circ}\text{C}$ and $\text{H}_2\text{O}/\text{C} = 0.3$.

Table 10

Comparison of the T-SOFC and P-SOFC based systems at maximum power density.

T_{ref} ($^{\circ}\text{C}$)	$\text{H}_2\text{O}/\text{C}$	System	Current density, j (mA cm^{-2})	AC efficiency at maximum current density (%)	Maximum AC power (kW)
700	0.5	T-SOFC	300	29.4	6.1
		P-SOFC	450	27.2	8.3
800	0.3	T-SOFC	300	26.3	6.0
		P-SOFC	450	23.2	7.8

the system at low or higher current density regions, respectively. If the system operates at a lower current density, efficiency will be higher necessitating a larger stack incurring higher initial capital cost. On the other hand if the system operates at a higher current

density, higher power can be obtained from a relatively smaller stack but sacrificing system efficiency and thus incurring relatively higher operating cost. Based on this study, the recommended operating window is given in Table 8.

4.4. Comparison between T-SOFC and P-SOFC based systems

Finally, the performance of the 5 kW_e P-SOFC based system was compared against previously published 5 kW_e T-SOFC based system [1] to see their relative advantages over one another operating at different current densities based upon equal total active cell area. The T-SOFC stack temperature was maintained at $910\text{ }^{\circ}\text{C}$ whereas the P-SOFC was maintained at $850\text{ }^{\circ}\text{C}$. Two different reformer temperatures e.g. $700\text{ }^{\circ}\text{C}$ and $800\text{ }^{\circ}\text{C}$ were selected to evaluate consistency of the results at $\text{H}_2\text{O}/\text{C}$ ratio of 0.5 and 0.3, respectively. Table 9 shows the input conditions for both systems.

Fig. 19 demonstrates the variation of cell voltage and net AC efficiency with current density for T- and P-SOFC based systems. Even though the P-SOFC based system was operating $60\text{ }^{\circ}\text{C}$ lower than the T-SOFC based system, superior cell voltage was obtained at relatively higher current densities for P-SOFC system. Higher operating temperature of the T-SOFC based system significantly reduced the activation voltage loss but it was not able to operate at higher current densities due to its longer circumferential current path causing higher ohmic loss. Conversely, planar geometry showed substantially less ohmic loss but the total voltage loss was dominated by the activation loss due to relatively lower temperature operation already discussed in Fig. 17. Fig. 20 presents the total voltage loss of the T- and P-SOFC based systems with current density. Unlike tubular cells, planar cells can operate at relatively higher current density due to lower total voltage loss. Due to this capability of higher current density operation, the P-SOFC based system was capable of achieving higher power density (at current densities above 200 mA cm^{-2}) with relatively higher efficiency compared to the T-SOFC system with identical cell area as presented in Figs. 19 and 21 at a representative ATR temperature of $800\text{ }^{\circ}\text{C}$.

Table 10 demonstrates that the P-SOFC based system can achieve a maximum AC power of 8.3 kW_e with a net AC efficiency of 27.2%, while the T-SOFC based system can achieve only 6.1 kW_e power with a net AC efficiency of 29.40% at $T_{ref} = 700\text{ }^{\circ}\text{C}$. This means for the same size stack, the P-SOFC based system can produce 2.2 kW_e more power than T-SOFC based system sacrificing 2.2% efficiency. Increased reformer temperature clearly decreased net AC power, still the P-SOFC based system showed superior performance in terms of power over the T-SOFC based system. This advantage of planar cell based system over tubular cell based system can be very attractive while operating the system at higher loads for MEP applications. Figs. 19–21 can be useful to make a decision of optimum operating condition considering a trade-off between efficiency and power density by analyzing the cell voltage, net AC efficiency and power requirements. Table 11 presents a range of optimum operating range scenario of the two systems which suggests that in order to produce a required power output the P-SOFC based system will require less cell area making the system smaller and lighter requiring less capital investment

Table 11

Optimum operating range of the T-SOFC and P-SOFC systems.

T_{ref} ($^{\circ}\text{C}$)	System	j (mA cm^{-2})	Cell voltage (V)	$\eta_{el,net}$ (%)	P_{ac} (kW)	Power density (mW cm^{-2})
700	T-SOFC	175–225	0.68–0.61	40.6–36.2	4.85–5.58	109.8–126.3
	P-SOFC	250–325	0.61–0.55	36.15–32.2	6.25–7.30	141.45–165.50
800	T-SOFC	175–225	0.68–0.61	37.67–33.50	4.83–5.55	109.34–125.70
	P-SOFC	250–325	0.60–0.53	32.90–29.30	6.1–7.1	137.80–160.14

compared to a T-SOFC system. However, at variable load conditions at higher current densities (above 200 mA cm^{-2}) the P-SOFC system can provide power more efficiently compared to the T-SOFC based system with the same size stack (also shown in Fig. 19).

At the end, it should be mentioned here that the study might contain some uncertainty due to simplified isothermal assumptions of ATR and SOFC operations. Another source of uncertainty is associated with temperature dependent material properties to calculate ohmic loss, pre-exponential factor and activation energy values to calculate activation loss, which were obtained from available literature. The fuel dilution may have some effect on concentration loss as well. It is difficult to quantify the uncertainty associated with material properties for this kind of study due to the limitation of dimensionality and unavailability of enough experimental data in open literature. Nevertheless, we believe that the Aspen Plus model achieved a good agreement in validating several studies from literature and made the current model quite acceptable.

5. Conclusion

The JP-8 fuel operated P-SOFC based system model revealed some important design criteria through this study. ATR characterization was shown to be an important step and was performed by varying the $\text{H}_2\text{O}/\text{C}$ ratio and ATR operating temperature. Increasing $\text{H}_2\text{O}/\text{C}$ and reformer operating temperature both helped suppress coke formation but at the same time increased fuel dilution. This caused decay of Nernst voltage and efficiency. The coke free operating region was evaluated at a minimum $\text{H}_2\text{O}/\text{C}$ ratio of 0.4, 0.25 and 0.15 at the respective ATR operating temperatures of 700°C , 750°C and 800°C . Better performance was observed at lower $\text{H}_2\text{O}/\text{C}$ ratio and ATR operating temperature zone. The system showed a maximum cell voltage of 640 mV at $T_{\text{ref}} = 700^\circ\text{C}$ with net AC efficiency of 37.1% at $\text{H}_2\text{O}/\text{C} = 0.4$ and a minimum cell voltage of 510 mV at $T_{\text{ref}} = 800^\circ\text{C}$ with net AC efficiency of 29.2% at $\text{H}_2\text{O}/\text{C} = 1.0$. The maximum and minimum total efficiency of the system were 70.2% and 61.7% at the lowest and highest ATR operating temperatures at $\text{H}_2\text{O}/\text{C}$ ratio of 0.4 and 1.0, respectively.

The parametric analyses showed that fuel utilization was another important parameter and higher fuel utilization required less fresh JP-8 fuel leading to higher net AC efficiency but at the same time thermal efficiency decreased due to less availability of unburned fuel at the post-combustor. On the other hand, operating the system at higher current density leads to lower cell voltage and net AC efficiency attributed by higher parasitic power loss. The P-SOFC based system obtained a peak power density of 188.5 mW cm^{-2} operating at a current density of 475 mA cm^{-2} with

$T_{\text{ref}} = 700^\circ\text{C}$, $\text{H}_2\text{O}/\text{C} = 0.5$ and 180.5 mW cm^{-2} operating at a current density of 450 mA cm^{-2} with $T_{\text{ref}} = 800^\circ\text{C}$, $\text{H}_2\text{O}/\text{C} = 0.3$.

Finally, the comparison study between a 5 kW_e P- and T-SOFC based systems was performed based on identical total cell area at ATR operating temperatures of 700°C and 800°C and $\text{H}_2\text{O}/\text{C}$ ratio of 0.5 and 0.3, respectively. P-SOFC based system was able to operate at higher current density which translated into higher power density due to lower ohmic loss. This means for the same size stack, P-SOFC based system can produce more power than the T-SOFC based system. Optimum operating range of the two systems has also been identified through this study.

Acknowledgments

The authors would like to acknowledge and appreciate Ohio Coal Research Center (OCRC) for their funding and other logistic support in completing this research.

References

- [1] T. Tanim, D.J. Bayless, J.P. Tremblay, J. Power Sources 221 (2013) 387–396.
- [2] M. Li, J.D. Powers, J. Brouwer, J. Fuel Cell Sci. Technol. 7 (2010), 041017-1–041017-12.
- [3] P. Kazempoor, V. Dorer, F. Ommi, Fuel Cells 10 (6) (2010) 1074–1094.
- [4] A. Musa, M. De Paepe, Int. J. Hydrogen Energy 33 (2008) 4665–4672.
- [5] S.C. Singhal, K. Kendall, High Temperature Solid Oxide Fuel Cells: Fundamentals, Design and Applications, Elsevier Ltd., Oxford, UK, 2003.
- [6] A.S. Patil, T.G. Dubois, N. Sifer, E. Bostic, K. Gardner, M. Quah, C. Bolton, J. Power Sources 136 (2004) 220–225.
- [7] J.D. Stangl, R.O. Wertz, F.H. Holcomb, Military Requirements of JP-8 Fuel Reformers and Solid Oxide Fuel Cell Power Systems, Engineering Research and Development Center-Construction Engineering Research Lab, 2005. ERDC/CERL TR-05-36.
- [8] N. Lutsey, C.J. Brodrick, D. Sperling, H.A. Dwyer, J. Transp. Res. Board 3443 (2003) 118–126.
- [9] M. Santarelli, M. Cabrera, M. Cali, J. Fuel Cell Sci. Technol. 7 (2010), 021006-1–021006-11.
- [10] W. Doherty, A. Reynolds, D. Kennedy, Energy 35 (2010) 4545–4555.
- [11] W. Zhang, E. Croiset, P.L. Douglas, M.W. Fowler, E. Entchev, Energy Convers. Manag. 46 (2005) 181–196.
- [12] S. Campanari, P. Iora, J. Power Sources 132 (2004) 113–126.
- [13] S. Campanari, J. Power Sources 92 (2001) 26–34.
- [14] C.O. Colpan, I. Dincer, F. Hamdullahpur, Int. J. Energy Res. 32 (2008) 336–355.
- [15] S.H. Chan, K.A. Khor, Z.T. Xia, J. Power Sources 93 (2001) 130–140.
- [16] P. Costamagna, A. Selimovic, M.D. Borghi, G. Agnew, Chem. Eng. J. 102 (1) (2004) 61–69.
- [17] J. Sadhukhan, Y. Zhao, N. Shah, N.P. Brandon, Chem. Eng. Sci. 65 (2010) 1942–1954.
- [18] Toxicological Profile Information Sheet, Agency for Toxic Substances and Disease Registry, Georgia, 2011 available at: <http://www.atsdr.cdc.gov/toxprofiles/tp121-c3.pdf> (accessed, 11.05.11).
- [19] J. Van herle, F. Maréchal, S. Leuenberger, D. Favrat, J. Power Sources 118 (2003) 375–383.
- [20] D. Liu, T.D. Kaun, H. Liao, S. Ahmed, Int. J. Hydrogen Energy 29 (2004) 1035–1046.